Int J Adv Manuf Technol (2016) 87:1685–1692
DOI 10.1007/s00170-016-8579-3

ORIGINAL ARTICLE

Microstructure and tensile properties of laser welded dissimilar Ti-22Al-27Nb and TA15 joints

Kezhao Zhang[1] · **Longchang Ni**[1] · **Zhenglong Lei**[1] · **Yanbin Chen**[1] · **Xue Hu**[1]

Received: 6 November 2015 / Accepted: 2 March 2016 / Published online: 10 March 2016

Abstract The laser weldability of dissimilar Ti-22Al-27Nb and TA15 joints was investigated. Some layered textures in the fusion zone were characterized. The heat-affected zone of TA15 was divided into two regions based on the phase compositions: $\beta+\alpha'$, $\beta+\alpha'+\alpha$, with increasing distance to the fusion line. Similarly, three different regions in the heat-affected zone of Ti-22Al-27Nb were identified: B2, B2 + α_2, and B2 + α_2 + O. The fusion zone was composed of B2 + α' dual phases, resulting from the chemical compositions of the fusion zone and rapid cooling rate of the laser welding process. Following tensile tests, the failure occurred in the weld at room temperature, while in the TA15 alloy at 650 °C. The fracture surface was examined, revealing features of quasi-cleavage fracture at room temperature and ductile fracture at 650 °C.

Keywords Laser welding · Dissimilar joints · Ti-22Al-27Nb and TA15 · Microstructure and properties

1 Introduction

Ti_2AlNb-based alloys, containing a large amount of the O (Ti_2AlNb) phase, are known as promising materials for aviation industry [1–6]. Developing from the conventional titanium aluminide Ti_3Al (α_2), Ti_2AlNb-based alloys are usually composed of O (orthorhombic, Ti_2AlNb), α_2 (hexagonal, Ti_3Al), and B2 (body-centered cubic) phase. The addition of Nb element has a beneficial effect on the room and high temperature properties. Compared to the classical titanium alloys such as TC4, Ti_2AlNb-based alloys have better antioxidant capacity and creep resistance at elevated temperatures. However, the cost of using Ti_2AlNb-based alloys to produce aviation components also increases with the addition of Nb element. Despite their balanced room and high temperature properties, the applications of Ti_2AlNb-based alloys are still restricted by the prohibitive cost. One way to reduce the cost is only using the Ti_2AlNb-based alloys for the critical parts. For example, the air inlet housing, made of TA15 (Ti-6Al-2Zr-1Mo-1 V, at.%), are designed to have built-in stop collars which are made of Ti_2AlNb-based alloys to resist high temperature oxidation. TA15 is a near-α titanium alloy with high specific strength, thermal stability, good weldability, and in mass production and is now widely used in aviation industry [7–9]. The applications of Ti_2AlNb-based alloys could be further promoted by combining to the TA15 alloy. Therefore, it is necessary to investigate the microstructure and mechanical properties of the dissimilar joints of Ti_2AlNb-based alloys and TA15.

As a high-energy beam welding method, laser welding has been increasingly widely used in recent years because of the high welding efficiency, low heat input, and high flexibility [10–12]. In spite of this, there are very limited research concerning the laser welding process of Ti_2AlNb-based alloys, not to mention the dissimilar metal laser welding process of Ti_2AlNb-based alloys and TA15. Most research focused on the laser welding process of Ti_3Al-based alloy, a potential structural material at modest temperature, but of which the applications are restricted by their poor machining properties and room temperature brittleness [13–16]. For joining the Ti_2AlNb-based alloy to itself, Dong et al. investigated the microstructure evolution and tensile properties of laser welded

✉ Zhenglong Lei
leizhenglong@hit.edu.cn

[1] State Key Laboratory of Advanced Welding and Joining, Harbin Institute of Technology, Harbin 150001, China

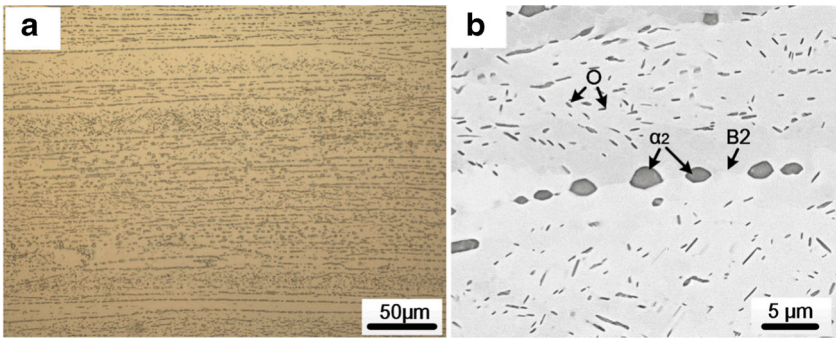

Fig. 1 Microstructure of the Ti-22Al-27Nb alloy. **a** Optical microscopy image and **b** backscattered electron image

Ti-22Al-27Nb (at.%) joints. The tensile strength and elongation-to-failure of single-B2-phased joints were approximately 1000 MPa and 6 % at room temperature, 733 MPa and 2.9 % at 650 °C [17]. The research on the dissimilar metal laser welding process of Ti-22Al-27Nb and TC4 showed that the tensile strength could reach 90 % of TC4 parent metal. However, the high temperature tensile properties of the dissimilar joints were not discussed [18]. There have been very rare reports of the laser welding process of Ti_2AlNb-based alloys and TA15 up till now. The aim of this investigation is to explore the laser weldability of dissimilar Ti_2AlNb and TA15 joints, including the microstructure evolution and room and high temperature tensile properties.

2 Experimental

The two base metals used for the experiment were 2.5 mm Ti_2AlNb-based alloy (Ti-22Al-27Nb, at.%) and TA15 sheets. The hot-rolled microstructure of Ti-22Al-27Nb is shown in Fig. 1. Figure 1a presents the overall microstructural characteristics of Ti-22Al-27Nb. Three different phases, spherical α_2, rod-shaped O, and the substrate B2 phase were marked in Fig. 1b. The as-cast microstructure of TA15 is shown in Fig. 2. Figure 2a shows the lamellar morphology of TA15. The gray regions and light regions were referred to as α and β phase, respectively, as marked in Fig. 2b. The chemical compositions of Ti-22Al-27Nb and TA15 are listed in Tables 1 and 2, respectively.

The workpieces were cut into 80 × 30 mm sections with wire electrical discharge machining (WEDM). Before welding, any oil stains or oxide layers were removed from the surface of workpieces with stainless steel brush polishing and a specific acid solution (30 % HNO_3, 3% HF, and 67 % H_2O). The to-be-welded sections were cleaned by acetone and water and dried in an oven at 80 °C for 1 h. Laser welding process was carried out using a 3 kW diffusion cooling carbon dioxide laser (ROFIN-SINAR DC030). The pre-optimized welding parameters were laser power 1800 W, welding speed 0.5 m/min, and laser defocus distance 0 mm. In order to minimize the oxidation of the welds, the laser welding process was conducted in an inert atmosphere of argon. Both shielding gas and back gas were adopted, and the flow rate for each was 15 and 10 l/min, respectively.

Metallographic specimens were cut out transversely from the welds and prepared following the standard metallographic

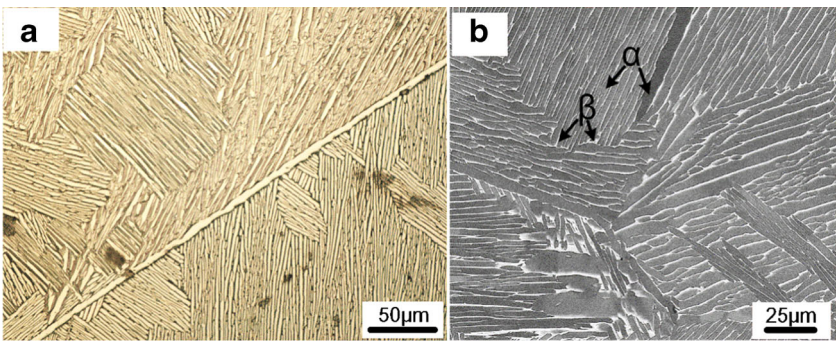

Fig. 2 Microstructure of the TA15 alloy. **a** Optical microscopy image and **b** backscattered electron image

Table 1 Chemical compositions of Ti-22Al-27Nb alloy (wt%)

Al	Nb	V	Ti
10.62	45.22	5.42	Balance

Table 2 Chemical compositions of TA15 alloy (wt%)

Al	Zr	Mo	V	Ti
7.45	3.11	2.47	0.78	Balance

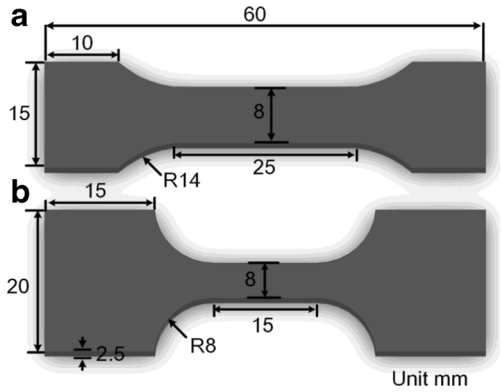

Fig. 3 Geometry of the tensile specimens at **a** room temperature and **b** 650 °C

procedures for titanium alloys, including grinding, polishing, and etching with a Kroll solution (3 % HF, 5 % HNO_3, and 92 % water). The optical microscopy (OM, VHX-1000E) and scanning electron microscopy (SEM, Helios 600i) were used to analyze the microstructural characteristics. The compositional analysis of the fusion zone was conducted using an energy dispersive spectrometer (EDS) on the SEM (Helios 600i). X-ray diffraction (XRD, D/MAX-RB) was used to identify the phase composition of the fusion zone. A slice sample was cut out of weld seam, mechanically polished, and ion-thinned for transmission electron microscopy analysis (TEM, Tecnai G2 F30). The tensile properties of the joints were evaluated with the Instron tensile testing machines at room temperature and 650 °C, at a displace speed of 1 mm/min. The geometry of the tensile specimens is shown in Fig. 3.

3 Results and discussion

3.1 Weld observations

Figure 4 shows the uniform and continuous Ti-22Al-27Nb and TA15 weld seam. When the titanium alloys were fusion welded without appropriate protection methods, a purple or gray oxide layer could be observed. It would cause a significant loss of the mechanical properties of the joints. The silvery weld bead and weld root indicated that the weld metal was well protected from oxidation. No obvious defects such as cracks or discontinuities are found according to Fig. 4a, b.

Figure 5 presents the macro- and micrographs of the laser welded Ti-22Al-27Nb and TA15 joints. As shown in Fig. 5a–c, some layered textures could be observed in the fusion zone. Similar phenomenon was also reported by other researchers [13, 14, 19]. The layered textures resulted from the release of latent heat during the crystallization process of the welding pool [20]. It was also noticeable that in the upper weld, the layered textures were semi-circular, while in the lower weld, the layers were linear. This was attributed to the difference in heat transfer direction between the upper and lower welds. When the welding was started but before penetrating the workpiece, the heat transferred in both the transverse and depth direction, resulting in the semi-circular layered textures. Following the penetration of the workpiece, a deep vapor cavity (known as the keyhole) was formed, and the heat transferred only in the transverse direction, resulting in the linear layered textures.

3.2 Microstructure of the heat-affected zone

The microstructure of the heat-affected zone (HAZ) of TA15 is shown in Fig. 6. Figure 6a shows the overall microstructural characteristics of the HAZ. With increasing distance to the fusion line, the microstructure of the HAZ from martensitic $\alpha' + \beta$ dual phases to primary α + martensitic $\alpha' + \beta$ three phases. According to the Ti-6Al-xV phase diagram, the phase transformation sequence was $\alpha \rightarrow \alpha + \beta \rightarrow \beta$ as the temperature increased [21]. In the near-HAZ, adjacent to the fusion line, the peak temperature was lower than the melting point but higher than the β transus. The primary α phase in the base metal, therefore, entirely transformed to the β phase on heating. Following the cooling process, the common $\beta \rightarrow \alpha$ transformation did not occur because of the very fast cooling rate in laser welding. Instead, the β phase transformed from the bcc structure to the hcp-structured phase, i.e., the martensitic α' phase, in a non-diffusional manner. The martensitic α' phase had the same chemical composition as the parent β phase. The morphology of needle-shaped α' phase is shown in Fig. 6b, where the primary lamellar morphology could hardly be observed. In the far-HAZ, farther from the fusion line, the temperature was lower than the near-HAZ. Consequently, the primary α phase only partially transformed to the β phase. The $\alpha + \beta$ lamellar structure was able to be

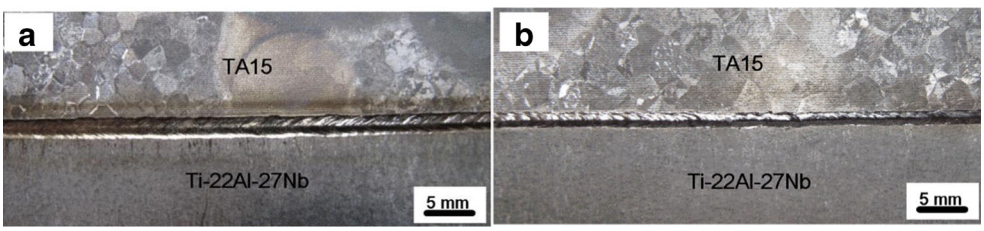

Fig. 4 Weld appearance of the laser welded Ti-22Al-27Nb and TA15 joints. **a** Weld bead. **b** Weld root

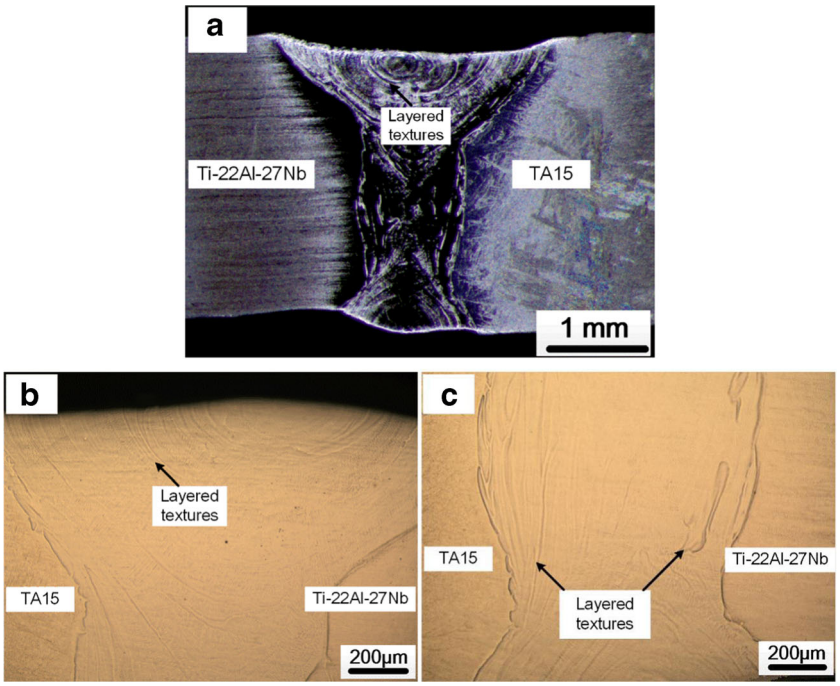

Fig. 5 Optical micrographs of laser welded Ti-22Al-27Nb and TA15 joints. **a** Macrostructure of the joint, **b** upper weld, and **c** lower weld

retained. The β → α′ transformation only occurred within the primary β phase, as shown in Fig. 6c.

Figure 7 shows the microstructure of the HAZ of Ti-22Al-27Nb. The microstructure of the HAZ also

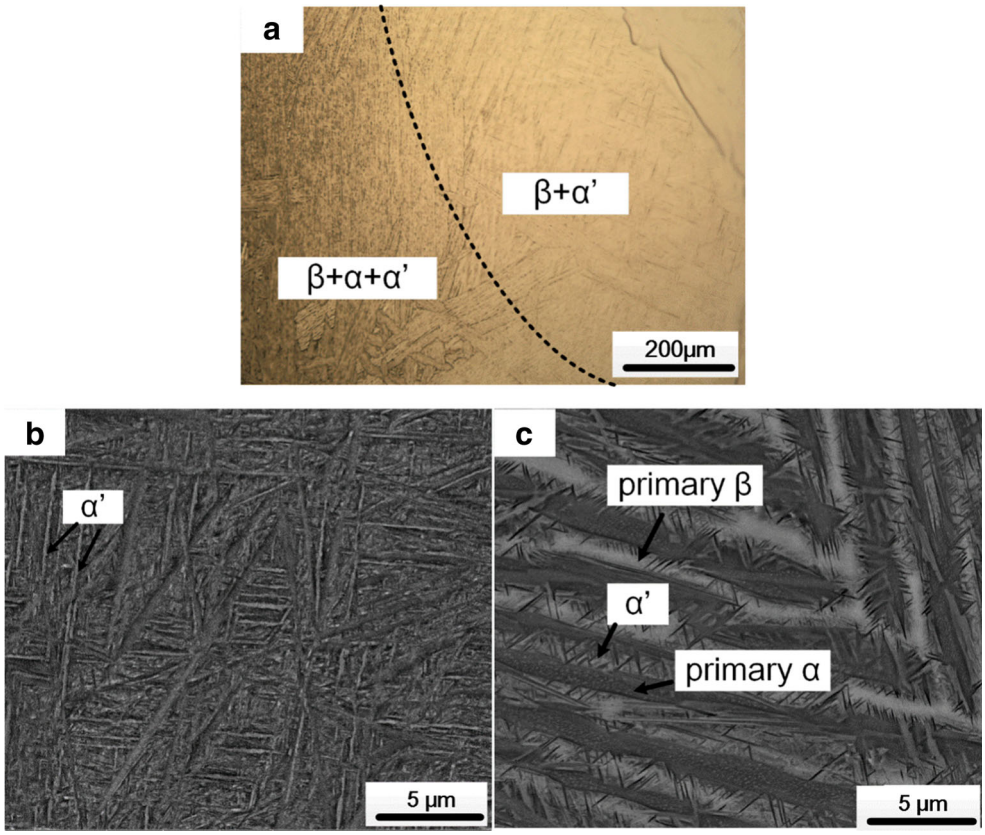

Fig. 6 Microstructure of the HAZ of TA15. **a** Optical microscopy image of the HAZ, **b** the acicular α′ phases in the near-HAZ, and **c** the transformed α′ phases within the primary β phase in far-HAZ

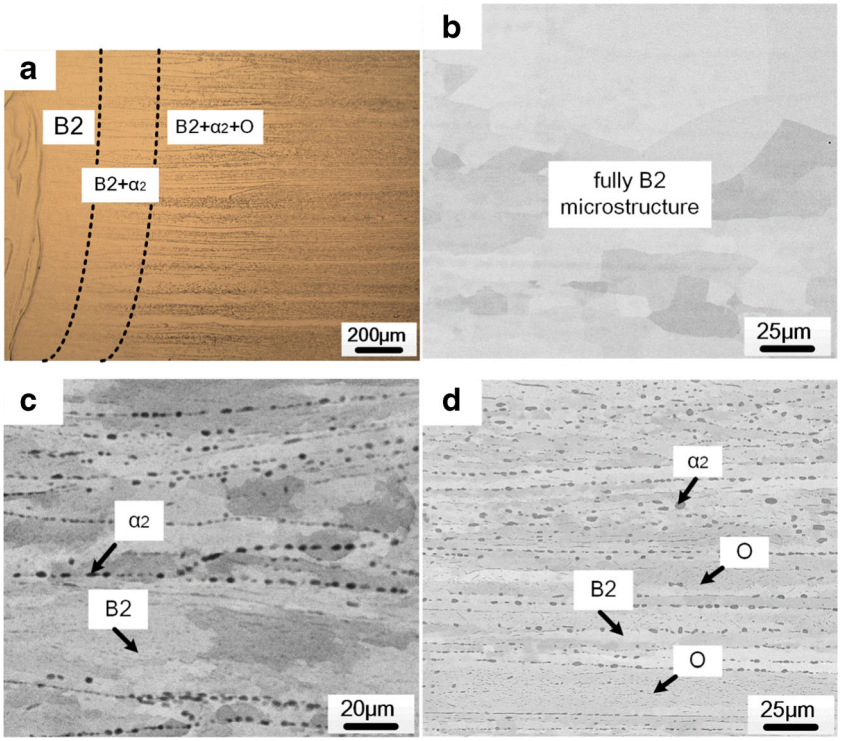

Fig. 7 Microstructure of the HAZ of Ti-22Al-27Nb. **a** Optical microscopy image of the HAZ, **b** BSE image of the single B2 phase region, **c** BSE image of the B2 + α_2 region, and **d** BSE image of the B2 + α_2 + O region

changed with the distance to the fusion line. For the Ti_2AlNb-based alloys, the phase transformation sequence was B2 + O → α_2 + B2 + O → B2 + α_2 → B2 as the temperature increased, according to the Ti-22Al-xNb phase diagram [22]. Accordingly, three different regions: single B2, B2 + α_2, and α_2 + B2 + O were indicated in the HAZ of Ti-22Al-27Nb, as shown in Fig. 7a. Closest to the fusion line was the single phase region, consisting of only B2 phase, where the peak temperature was lower than the melting point but higher than the B2 transus. Both the α_2 phase and O phase transformed to B2 phase on heating. The phase transformation rate of α_2 or O → B2 was quite fast because the B2 phase had a higher diffusivity due to its less densely packed structure [21]. Following the cooling process, the decomposition of B2 to α_2 or O phase was entirely suppressed by the rapid cooling rate. This was because the B2 → α_2 or O transformation was a diffusion controlled process. Moreover, both the α_2 and O phase had a close-packed crystal structure, leading to a low self-diffusion coefficient. If cooled from above the B2 transus slowly enough, the final microstructure would be a mixture of B2, α_2, and O phase. However, the cooling rate in laser welding was too fast to trigger the transformation. Therefore, a single B2 phase region was formed, as shown in Fig. 7b. Farther to the fusion line was the B2 + α_2 region, where the peak temperature dropped. Only the O → B2 transformation occurred and the primary α_2 phase was retained, as shown in Fig. 7c. Adjacent to the unaffected base metal was the α_2 + B2 + O region, where the peak temperature continued dropping with increasing distance to the fusion line. The phase transformation could hardly occur with such low temperature, and the microstructure of this region remained the almost same as the base metal, as shown in Fig. 7d.

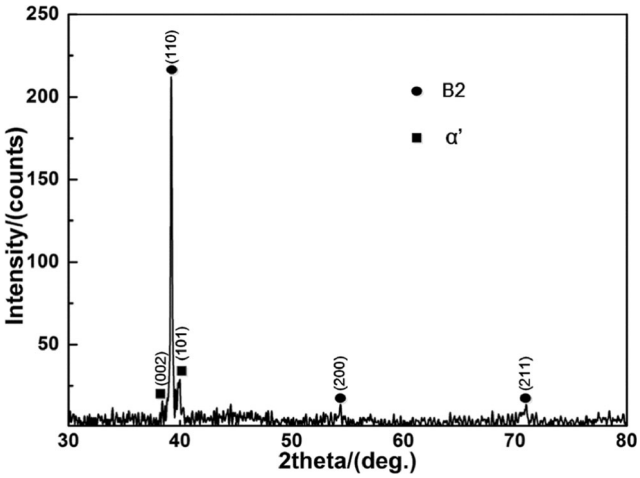

Fig. 8 XRD analysis of the fusion zone

3.3 Microstructure of the fusion zone

The microstructural characteristics of the fusion zone are presented in Figs. 8 and 9. The diffraction peaks referring to the α′ phase and B2 phase were annotated in

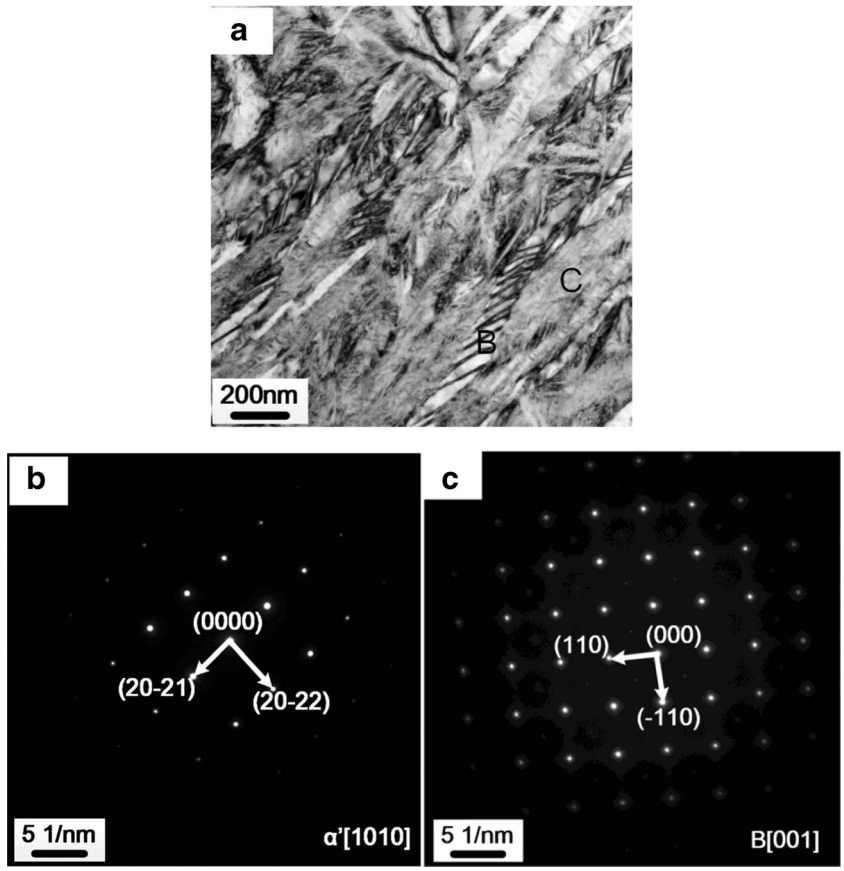

Fig. 9 TEM analysis of the fusion zone. **a** The bright field image of the fusion zone. The corresponding SAED patterns of the **b** α′ phase and **c** B2 phase

Fig. 8. The results of TEM analysis are shown in Fig. 9. The acicular α′ phase and B2 phase could also be observed in the bright field image, as shown in Fig. 9a. The corresponding selected area diffraction patterns (SADPs) of α′ phase and B2 phase are shown in Fig. 9b, c.

When joining the Ti_2AlNb-based alloy to itself, it has been well established that the fusion zone of laser welded joints was composed of single B2 phase [17]. However, in this case, the fusion zone of laser welded dissimilar Ti-22Al-27Nb and TA15 joints was composed of α′ + B2 dual phases. The dual-phase microstructure resulted from the chemical compositions in the fusion zone. The major alloying elements of the fusion zone were Al and Nb, both of which had significant effects on phase transformation. It has been widely acknowledged that Nb worked as β phase stabilizer during phase transformation. A high Nb content promoted the formation of fully B2 microstructure. While the Al element, usually working as α phase stabilizer, promoted the formation of α phase. As listed in Table 1, the Nb:Al ratio (in wt%) of Ti-22Al-27Nb is 4:1. As a consequence, the fusion zone of laser welded Ti-22Al-27Nb joints had a fully B2 microstructure because of the relatively high Nb:Al ratio. The EDS results of the fusion zone of the dissimilar Ti-22Al-27Nb and TA15

Table 3 EDS results of the fusion zone (wt%)

Al	Nb	Mo	V	Zr	Ti
8.12	20.55	1.38	0.95	1.51	Balance

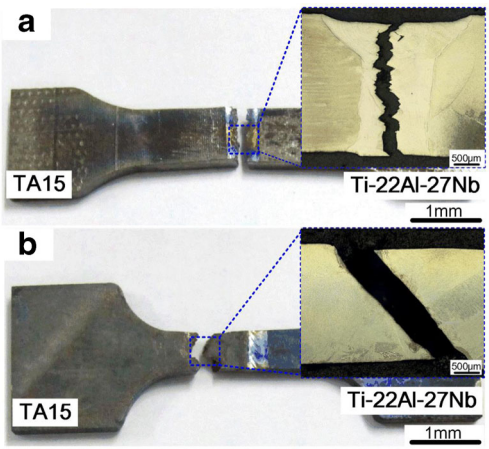

Fig. 10 The photographed fractured specimens after tensile tests at **a** room temperature and **b** 650 °C

Table 4 Tensile properties of laser welded Ti-22Al-27Nb/TA15 joints at room temperature

	Tensile strength (MPa)	Elongation-to-failure (%)
1	900.6	2.5
2	870.4	3.6
3	893.2	2.1

Table 5 Tensile properties of laser welded Ti-22Al-27Nb/TA15 joints at 650 °C

	Tensile strength (MPa)	Elongation-to-failure (%)
1	401.9	6.7
2	425.1	6.0
3	439.7	4.8

joints is shown in Table 3. The Nb:Al ratio (in wt%) of the fusion zone is approximately 2.5:1, much lower than that of Ti-22Al-27Nb. Therefore, the low Nb, high Al content of the fusion zone tilted the balance in favor of the formation of α phase. Similar to the phase transformation occurring in the HAZ of TA15, the martensitic α′ phase was generated due to the fast cooling rate. The transformed α′ phase also took the needle shape, as shown in Fig. 9a.

3.4 Tensile properties

The photographed fractured specimens after the tensile tests are shown in Fig. 10. The fracture occurred in the weld, in the room temperature tested specimen, and in the TA15 alloy, in the high temperature tested specimen, as shown in Fig. 10b, c.

The room temperature tensile properties of Ti-22Al-27Nb and TA15 dissimilar joints are shown in Table 4. Both the ultimate tensile strength and elongation-to-failure of laser welded dissimilar Ti-22Al-27Nb and TA15 joints were lower than the reported laser welded Ti-22Al-27Nb joints [17]. The loss of the strength and ductility of dissimilar joints was caused by the α′ phase in the fusion zone. The acicular α′ phase, having a hexagonal close-packed structure, was brittle and incapable of blocking the propagation of cracks. The large amount of α′ phases inhibited the dislocation motion and provided crack initiation sites, leading to the premature fracture and lower elongation-to-failure of the dissimilar joints. The fracture surface of the dissimilar joints at room temperature is shown in Fig. 11. The quasi-cleavage fracture features could be characterized from the ductile dimples and cleavage step patterns, as shown in Fig. 11a. The cleavage steps in Fig. 11b were ascribed to the large amount of α′ phases in the interior of grains. The cracks tended to initiate and propagate within the α′ phase or along the α′/α′ boundaries during tensile deformation. Figure 11c shows there also existed an amount of ductile dimples on the fracture surface. The ductile dimples mainly resulted from the tearing ridge of B2 phase, which had a body-centered cubic lattice and more slip systems than the hexagonal α′ phase.

The tensile properties of laser welded dissimilar Ti-22Al-27Nb and TA15 joints at 650 °C are shown in Table 5. The fracture occurred in the TA15 base metal

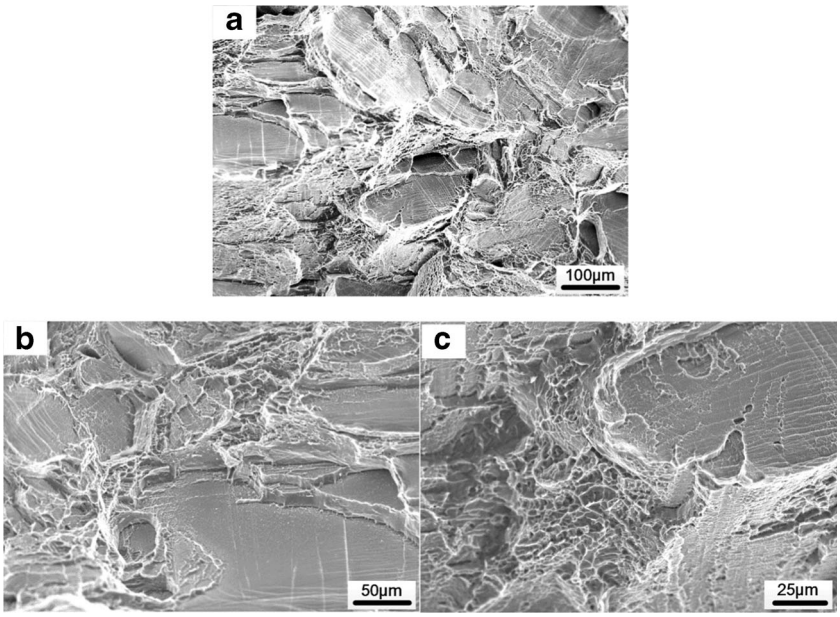

Fig. 11 The fracture surface of laser welded Ti-22Al-27Nb and TA15 joints at room temperature. **a** The overall quasi-cleavage fracture features of the joints, **b** cleavage steps, and **c** ductile dimples

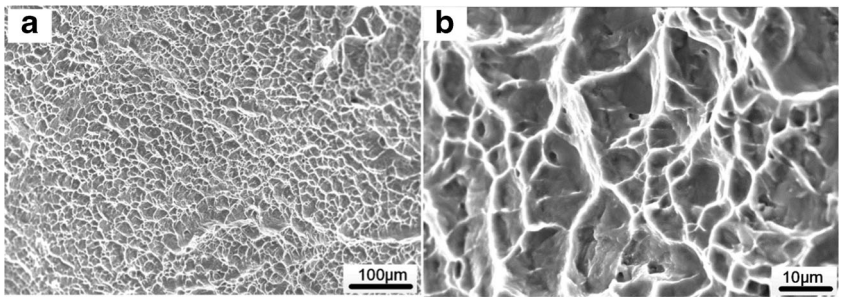

Fig. 12 The fracture surface of laser welded Ti-22Al-27Nb and TA15 joints at 650 °C. **a** Ductile dimples throughout the fracture surface. **b** A higher magnification of **a**

during testing. Figure 12 shows the fracture surface of 650 °C tested specimens. A typical ductile microvoid coalescence feature of the dissimilar joints could be identified with the dimples throughout the fracture surface. The hexagonal α' phase in the fusion zone were able to inhibit the dislocation motion even at very high temperatures. In the meanwhile, more slip systems became available in TA15 alloy at elevated temperatures, causing the increase of elongation-to-failure but significant decrease of ultimate tensile strength. Therefore, the failure occurred on the TA15 side of the joints at 650 °C because of its low strength.

4 Conclusion

(1) The dissimilar metal laser welding process of Ti-22Al-27Nb and TA15 was successfully applied and no defects were found in the weld.
(2) The microstructure of the HAZ of TA15 was characterized as $\beta+\alpha'$, $\beta+\alpha+\alpha'$ with increasing distance from the fusion line; similarly, the HAZ of Ti-22Al-27Nb was divided into three regions: single B2, B2 + α_2, and B2 + α_2 + O.
(3) The fusion zone was composed of B2 and acicular α' dual phases, resulting from the chemical compositions of the fusion zone and fast cooling rates in laser welding.
(4) The fracture was quasi-cleavage at room temperature, which was caused by the acicular α' phase and B2 phase in the fusion zone. The fracture at 650 °C was ductile microvoid coalescence and the failure was located on the TA15 side.

References

1. Rowe R (1992) Ti_2AlNb-based alloys outperform conventional titanium aluminides. Adv Mater Process 141:33–35
2. Banerjee D (1997) The intermetallic Ti_2AlNb. Prog Mater Sci 42: 135–158
3. Boehlert C, Majumdar B, Seetharaman V, Miracle D (1999) Part I. The microstructural evolution in Ti-Al-Nb O+ BCC orthorhombic alloys. Metall Mater Trans A 30:2305–2323
4. Lin P, He Z, Yuan S, Shen J (2012) Tensile deformation behavior of Ti–22Al–25Nb alloy at elevated temperatures. Metall Mater Trans A 556:617–624
5. Lin P, He Z, Yuan S, Shen J, Huang Y, Liang X (2013) Instability of the O-phase in Ti–22Al–25Nb alloy during elevated-temperature deformation. J Alloys Compd 578:96–102
6. Kumpfert J (2001) Intermetallic alloys based on orthorhombic titanium aluminide. Adv Eng Mater 3:851–864
7. Zhang D, Yang H (2013) Preform design for large-scale bulkhead of TA15 titanium alloy based on local loading features. Int J Adv Manuf Technol 67:2551–2562
8. Zhang D, Yang H, Li H (2012) Friction factor evaluation by FEM and experiment for TA15 titanium alloy in isothermal forming process. Int J Adv Manuf Technol 60:527–536
9. Zhan X, Wang Y, Liu Y, Zhang Q, Li Y, Wei Y (2015) Investigation on parameter optimization for laser welded butt joint of TA15 alloy. Int J Adv Manuf Technol 1-10.
10. Suder W, Ganguly S, Williams S, Paradowska A, Colegrove P (2011) Comparison of joining efficiency and residual stresses in laser and laser hybrid welding. Sci Technol Weld Join 16:244–248
11. Assunção E, Quintino L, Miranda R (2010) Comparative study of laser welding in tailor blanks for the automotive industry. Int J Adv Manuf Technol 49:123–131
12. Yoon S, Hwang J, Na S (2007) A study on the plasma-augmented laser welding for small-diameter STS tubes. Int J Adv Manuf Technol 32:1134–1143
13. Wang G, Zhao Y, Wu A, Zou G, Ren J (2007) Microstructure and high-temperature tensile properties of Ti_3Al alloys laser welding joint. Chin J Nonferrous Metals 17:1803
14. Wu A, Zou G, Ren J, Zhang H, Wang G, Liu X, Xie M (2002) Microstructures and mechanical properties of Ti–24Al–17Nb (at.%) laser beam welding joints. Intermetallics 10:647–652
15. Baeslack W, Mascorella T, Kelly T (1989) Weldability of a titanium aluminide. Weld J 68:483–498
16. Martin G, Albright C, Jones T (1995) An evaluation of CO2 laser beam welding on a Ti3Al-Nb alloy. Weld J 74:77–82
17. Lei Z, Dong Z, Chen Y, Zhang J, Zhu R (2013) Microstructure and tensile properties of laser beam welded Ti–22Al–27Nb alloys. Mater Des 46:151–156
18. Lei Z, Dong Z, Chen Y, Huang L, Zhu R (2013) Microstructure and mechanical properties of laser welded Ti–22Al–27Nb/TC4 dissimilar alloys. Mater Sci Eng A 559:909–916
19. Feng J, Wu H, He J, Zhang B (2005) Microstructure evolution of electron beam welded Ti3Al–Nb joint. Mater Charact 54:99–105
20. Zhang W (1996) Welding metallugy. China machine press, Beijing
21. Peters M, Hemptenmacher J, Kumpfert J, Leyens C (2003) Titanium and titanium alloys. Wiley-VCH Verlag, Germany
22. Raghavan V (2005) Al-Nb-Ti (aluminum-niobium-titanium). J Phase Equilib Diffus 26:360–368